J. Fluid Mech. (2002), *vol.* 462, *pp.* 133–159.
DOI: 10.1017/S0022112002008443 Printed in the United Kingdom

Experimental studies on the stability of Newtonian Taylor–Couette flow in the presence of viscous heating

By JAMES M. WHITE AND SUSAN J. MULLER†

Department of Chemical Engineering, University of California at Berkeley and Lawrence Berkeley National Laboratory, Berkeley, CA 94720, USA

(Received 25 April 2001 and in revised form 4 December 2001)

The dramatic effects of viscous dissipation on the stability of Newtonian Taylor–Couette (TC) flows are studied experimentally using flow visualization techniques. Viscous heating, parameterized by the Nahme–Griffith number *Na*, drives a transition to a new, oscillatory mode of instability when coupled with the effects of centrifugal destabilization. This instability, consisting of travelling axisymmetric vortices, only occurs when viscous heating and centrifugal destabilization are both present. Step tests in cylinder velocity show that the time following initiation of shearing required for onset of instability scales well with the time for the fluid to reach a steady temperature profile under the action of viscous heating. The onset time can be dramatically reduced at fixed *Na* by increasing the centrifugal destabilization through the addition of co-rotation of the outer cylinder. The onset time can also be reduced while holding the centrifugal destabilization constant by increasing the amount of viscous heating (i.e. holding Reynolds number *Re* constant while increasing *Na*). The effects of viscous heating on the critical conditions of Newtonian TC flows are also quantified using ramp tests in cylinder velocity. These tests reveal the large extent to which viscous heating is destabilizing; at $Na \approx 2$, a transition occurs at a critical *Re* that is less than 5% of the isothermal value.

1. Introduction

Recently there has been increased interest in the effects of viscous heating on the hydrodynamic stability of fluids. In addition to being of general interest to physicists, this subject is of great importance to the polymer processing industry, where highly viscous polymeric liquids under shear may experience a significant increase in temperature due to viscous dissipation. The dissipation-induced temperature gradient may interact with destabilizing forces to enhance the destabilization and reduce the useful operating window of polymer processing equipment. Viscous heating is also present in the processing of viscous, Newtonian fluids, and is known to affect the stability of flows of Newtonian fluids (Joseph 1965; Sukanek, Goldstein & Laurence 1973; White & Muller 2000; Al-Mubaiyedh, Sureshkumar & Khomami 1999, 2002).

Taylor–Couette flow, or flow between concentric, rotating cylinders, is a convenient starting point for examining the effects of viscous heating on hydrodynamic stability. This flow configuration and the relevant geometrical parameters are shown schematically in figure 1. This geometry has a simple, easily generated base flow and the

† Author to whom correspondence should be addressed: muller2@socrates.berkeley.edu

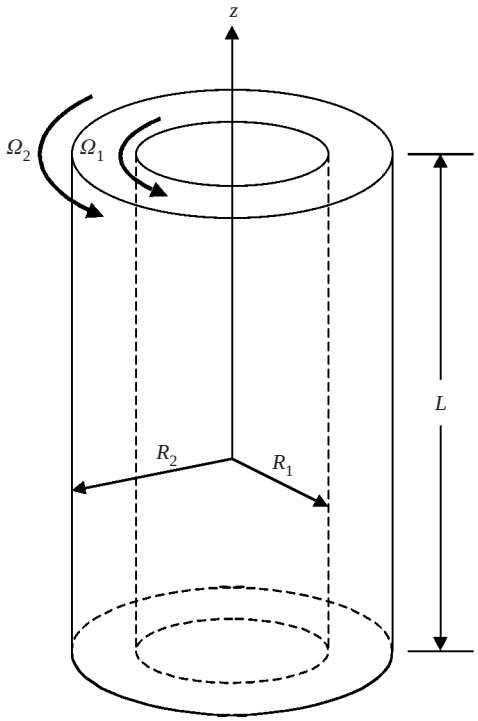

FIGURE 1. Schematic of Taylor–Couette flow.

recirculating nature of the flow makes it ideal for visualization experiments. In addition, the inherent symmetry of Taylor–Couette flow makes it a convenient platform for theoretical hydrodynamic stability studies. Here we report experimental studies on the effects of viscous heating on the hydrodynamic stability of Taylor–Couette (TC) flow of Newtonian fluids. The isothermal and non-isothermal hydrodynamic stability of Newtonian fluids is much better characterized and understood than that of viscoelastic fluids. In addition to providing a greater understanding of general hydrodynamic stability problems, we hope to apply the techniques and methodologies developed for these Newtonian experiments to more complex and industrially relevant flows of viscoelastic fluids.

In the isothermal TC flow of a Newtonian fluid, as the rotation rate of the inner cylinder is increased, the purely azimuthal base flow becomes unstable at a critical rotation speed and is replaced by stationary, axisymmetric vortices. The critical condition may be expressed as a critical Reynolds number ($Re_{c,iso}$); here we define the Reynolds number as $Re = |\Omega_2 - \Omega_1|R_1(R_2 - R_1)/\nu$, where R_1 and R_2 are the radii and Ω_1 and Ω_2 are the angular velocities of the inner and outer cylinders, respectively, and ν is the kinematic viscosity. As the rotation speed of the inner cylinder is further increased beyond the critical condition (i.e. for $Re > Re_{c,iso}$), the stationary axisymmetric vortices are replaced by increasingly complex flows through a now well-documented series of transitions (Andereck, Liu & Swinney 1986; Koschmieder 1993; Tagg 1994). Since this instability occurs due to centrifugal destabilization, the base flow remains stable when generated through rotation of the outer cylinder only. A co-rotation parameter B, defined as $B = (\Omega_2 - \Omega_1)/\Omega_1$, may be used to parameterize the extent of centrifugal destabilization. $B = -1$ represents rotation of the inner cylinder only and is the most frequently studied case.

A large number of dimensionless groups are necessary to completely describe nonisothermal Taylor–Couette flow of a Newtonian fluid. In addition to centrifugal forces (described by Re and B), the Prandtl number, which represents the ratio of momentum to thermal diffusivity, plays an important role in determining the stability behaviour. Defined as $Pr = C_p\eta/k$, where η is the shear viscosity, C_p is the heat capacity, and k is the thermal conductivity of the fluid, the Prandtl number is a function of temperature but is independent of other flow conditions (i.e. shear rate) in the apparatus. The effect of viscous heating is characterized by the Brinkman number, Br, which scales the viscous dissipation term in the energy equation. The Brinkman number is defined as $Br = \eta(R_1|\Omega_2 - \Omega_1|)^2/kT_0$, where T_0 is the wall temperature. Since the fluid viscosity may also be sensitive to temperature, the effects of the viscosity gradient can be accounted for through the Nahme–Griffith number, $Na = Br\Gamma$, where Γ is the thermal sensitivity of the viscosity, $\Gamma = |(T/\eta)(\partial\eta/\partial T)|_{T_0}$.

For large temperature differences across the gap or for large changes in density with temperature, buoyancy forces also become important in determining the stability characteristics. The ratio of buoyancy to viscous effects is parameterized by the Grashof number, defined as $Gr = g\beta d^3\Delta T/\nu^2$, where g is the acceleration due to gravity, β is the coefficient of thermal expansion of the fluid, d is gap between the cylinders ($R_2 - R_1$), and ΔT is the temperature change across the gap. ΔT is defined as ($T_{inner} - T_{outer}$) and thus is considered to be positive if the inner cylinder is hotter than the outer. For a viscous-heating-induced density stratification, the Grashof number can be found by setting ΔT equal to the maximum temperature increase in the gap. This quantity is equal to one eighth times the product of the Brinkman number and the absolute temperature. Finally, since the thermally induced density gradient may interact with both the centrifugal potential and the gravitational potential, the ratio of these two buoyancy forces will be important for large temperature gradients.

Previous work on the stability of non-isothermal Taylor–Couette flow has focused on the effect of an imposed radial temperature gradient (Snyder & Karlsson 1964; Sorour & Coney 1979; Ali & Weidman 1990; Chen & Kuo 1990). Both experiments and calculations have concentrated on the case of rotation of the inner cylinder only ($B = -1$). These studies show that small imposed radial temperature gradients have a modest effect on the flow stability, slightly increasing or decreasing the critical Re, depending on the magnitude of the Prandtl number and the magnitude of the temperature difference or, equivalently, the Grashof number Gr. These effects are described in more detail below.

Snyder & Karlsson (1964) studied the flow of water and glycerin–water solutions in a vertical TC apparatus with an imposed temperature difference between the cylinders. For $Pr \approx 5$ and for small temperature differences ΔT(i.e. $|Gr| < 40$), both positive and negative temperature gradients were found to stabilize the flow slightly. The stabilized secondary flow structures resembled those in the isothermal case: stationary, axisymmetric, toroidal cells. The maximum stabilization relative to the isothermal case was about 5%; that is, the critical condition corresponded to approximately $1.05Re_{c,iso}$. As the imposed temperature gradients were further increased, however, the flow was destabilized for both positive and negative temperature gradients. The secondary flow under these conditions was stationary, non-axisymmetric spiral cells. At the largest temperature differences reported, corresponding to $Gr \approx 400$, the critical conditions were approximately $0.90Re_{c,iso}$. The authors studied several flow conditions and the stability results were independent of fluid properties: stability curves could be plotted as universal curves of Re_c versus ΔT. Snyder & Karlsson speculated that the important effect of the temperature gradient is the addition of an axial flow due

to natural convection; it is this axial velocity which affects the stability of the base flow.

In subsequent experiments, Sorour & Coney (1979) studied the effect of an imposed temperature gradient on the TC stability of two oils. The imposed temperature gradient was found to be monotonically destabilizing and the form of instability was always stationary, axisymmetric, toroidal vortices. The maximum destabilization was approximately 84% of the isothermal critical condition (i.e. $Re_c \approx 0.84 Re_{c,iso}$) at a Grashof number of about 70. Once again this destabilization was attributed to the axial flow driven by natural convection. These authors did not, however, observe stabilization at small ΔT as found in Snyder & Karlsson's work. However, Sorour & Coney did not report Prandtl numbers for their oils and so the relevance of a direct comparison is not clear.

Ali & Weidman (1990) performed extensive stability calculations for Taylor–Couette flow with radial heating across the annulus and the cylinder axes aligned with gravity as in the experiments described above. A Boussinesq approximation was made to account for buoyancy arising from the interaction of the thermally induced density gradient and the gravitational potential. The stability was tested with respect to both axisymmetric (toroidal) and non-axisymmetric (helical) disturbances. Calculations at the specific conditions of the work of both Snyder & Karlsson and Sorour & Coney were performed to address the apparent conflicts between the two sets of experiments. Ali & Weidman demonstrated that increasing the Prandtl number decreases the system stability, and the effect increases markedly for $Gr > 30$. These authors' predictions are in qualitative agreement with the results of both Snyder & Karlsson and Sorour & Coney, the differences between the two sets of experiments being due primarily to Pr effects. (Ali & Weidman estimate $300 < Pr < 860$ for the latter experiments.) Thus, at low Gr either modest stabilization or destabilization of Re_c may be observed, depending on Pr. As Gr is increased from zero, the most unstable mode changes from an axisymmetric one to a non-axisymmetric mode. Dramatic destabilization relative to the isothermal critical condition is predicted only for high Gr.

Chen & Kuo (1990) also calculated the linear stability of Taylor–Couette flow with a small radial temperature gradient. Although they considered only axisymmetric disturbances, they examined the interaction of the thermally induced density gradient with both the centrifugal and the gravitational potentials. When buoyancy forces induced by the centrifugal potential are included, the stability curves are no longer symmetric about $Gr = 0$, i.e. increasing the ratio of centrifugal to gravitational buoyancy forces is stabilizing for $Gr > 0$ and destabilizing for $Gr < 0$. Like Ali & Weidman, they found that Pr has a large effect on the flow stability and it is possible to obtain the results of Snyder & Karlsson (stabilizing and then destabilizing as ΔT is increased) and Sorour & Coney (monotonically destabilizing in ΔT) by varying Pr. This suggests that the effect of thermal fluid properties is a large one, that both gravitational and centrifugal buoyancy must be taken into account, and that the stability landscape of non-isothermal TC flow is very complex.

The stability of Newtonian TC flow in which the non-isothermal effects are due to viscous dissipation, rather than an imposed temperature gradient, has received considerably less attention. Kolyshkin & Vaillancourt (1993) have performed linear stability calculations on the related case of Newtonian TC flows with temperature gradients caused by uniform heat generation in the fluid. As in Chen & Kuo's work, the fluid density is allowed to change with temperature and thus the temperature gradients cause buoyant secondary flows that ultimately lead to instability. In contrast to calculations for the case of radial heating however, for small gaps and for Prandtl

numbers from 1 to 100, Kolyshkin & Vaillancourt found that the most unstable disturbance flows were always axisymmetric, with larger amounts of heat generation and larger Pr causing increased destabilization.

For the most part, the theoretical and experimental studies of non-isothermal Newtonian TC flows have focused on fluids that have low Prandtl number ($Pr < 100$) and are near the threshold for the isothermal instability. A few studies, however, have been performed on more viscous fluids where temperature gradients may be caused by viscous dissipation. Al-Mubaiyedh *et al.* (1999, 2002) recently performed linear stability calculations on Newtonian fluids with much larger $Pr(\sim 11\,000)$. Thus, significant viscous heating was considered to be present in these flows. In these calculations, however, buoyancy is neglected and the viscous-heating-induced temperature gradient causes changes only in the viscosity. In this case, viscous heating was found to cause a new, axisymmetric mode of instability in Newtonian fluids. The mechanism of the new instability is a result of the coupling between the perturbation radial velocity and the base-state radial temperature gradient giving rise to an enhanced centrifugal force and a reduction in the critical Reynolds number. This mode of instability is stationary if the outer and inner cylinders are held at precisely the same temperature, and oscillatory with axially propagating vortices if the outer cylinder is slightly hotter than the inner. This new mode is monotonically destabilizing: as viscous heating – parameterized by the Brinkman number (or the Nahme–Griffith number) – is increased, dramatic destabilization from the isothermal TC flow critical conditions can be observed. These studies are particularly striking in that destabilization is predicted without the inclusion of buoyancy, which has been found to be the driving force for enhanced TC destabilization in all past theoretical studies.

The results of Al-Mubaiyedh *et al.* were confirmed qualitatively when a new mode of destabilization of Newtonian fluids by viscous heating was experimentally observed by White & Muller (2000). For the TC flow of glycerin, an axisymmetric, oscillatory instability was seen at Reynolds numbers as low as $0.126Re_{c,iso}$. In these experiments the outer and inner cylinders were held at the same temperature. These new secondary flows are much weaker than Taylor vortex flow and appear only after shearing the fluid at a constant Re for a very long time. The experimental apparatus and image analysis system, originally developed to examine weak elastic instabilities in viscoelastic Boger fluids (Baumert & Muller 1995), was very well-suited to examine these weak, low-Re, Newtonian instabilities.

In the present work we provide a comprehensive experimental investigation of this new viscous-heating-induced instability in Newtonian Taylor–Couette flow. In particular, we seek to understand how the instability is affected by the dimensionless groups and destabilizing forces present in the problem. The features of this instability are first examined using tests at fixed rotation rate to determine the temporal behaviour of the flow and verify our understanding of the relevant time scales in the problem. Using the information from the step tests to deduce an appropriate ramp speed, ramp tests are performed to determine the critical conditions. Care must be taken in the choice of appropriate ramp speed due to the longer time scale associated with the development of the thermal field than is inherent in the isothermal Newtonian problem. An inappropriate choice of ramp speed may cause misrepresentation of the critical conditions.

In all experiments presented, the temperature differences across the gap are small and $Gr < 0.6$. Based on the small Grashof number and the results of Al-Mubaiyedh *et al.* (1999, 2002), who find that variations in viscosity lead to instability in the

absence of buoyancy, we anticipate that destabilization is the result of variations in viscosity rather than density. For this reason, we report the magnitude of viscous heating in terms of the Nahme–Griffith number rather than the Brinkman number, since the latter does not reflect the thermal sensitivity of the viscosity. While we do not include explicitly the values of Br and Gr for all experiments, we include values for the thermal sensitivity of the viscosity Γ and the thermal sensitivity of the density β for all fluids and thus the Brinkman number and Grashof number may easily be calculated.

In general, the geometrical parameters of aspect ratio ($L/[R_2 - R_1]$) and radius ratio (R_1/R_2) also play an important role in determining the stability characteristics of the flow (De Roquefort & Grillaud 1978; Koschmieder 1993; Tagg 1994). No attempt, however, is made here to explore the effects of these geometrical parameters and results are reported only for two fixed values.

2. Experimental procedure

2.1. *Apparatus*

The experimental apparatus is shown schematically in figure 2. The fluid to be studied fills the gap between an anodized aluminium inner cylinder and a precision-bore glass outer cylinder. Two different inner cylinders may be used, one with a radius of 6.299 ± 0.001 cm, and the other with a radius of 6.946 ± 0.001 cm. The outer cylinder radius is 7.615 ± 0.003 cm, so the ratio of cylinder radii R_1/R_2 is 0.827 and 0.912 for the wide and narrow gap geometries, respectively. The total cylinder length is 40.6 cm, which gives a length/gap width ratio of 30.9 and 60.7 for the two geometries. The inner and outer cylinders can be independently rotated with microstepping motors having a resolution of 50 000 steps/revolution. The motors are computer-controlled, which allows for precise control and makes programming of arbitrary velocity profiles possible. The z-axis of the cylinders is aligned with gravity.

For all tests described herein, the outer and inner cylinders are held at equal temperatures. Since viscous heating only causes a very small temperature increase in the working fluid, the temperature of the inner and outer cylinders must be controlled carefully to keep extraneous or externally imposed temperature gradients from obscuring the experimental results. The temperature of the outer cylinder is controlled by placing the cylinders in a bath of recirculating light mineral oil that has the same index of refraction as the glass outer cylinder. In addition to temperature control, the bath fluid allows viewing of the test fluid through the curved glass surface without optical distortion. The inner cylinder temperature is maintained by pumping mineral oil through its baffled, hollow centre. This system allows both thermostatting fluid temperatures to be controlled to within ± 0.1 K. Although the temperatures of the thermostatting fluids may be controlled very accurately, the temperatures of these fluids may not correspond exactly to the wall temperatures. An increase in the test fluid temperature due to viscous heating may cause the wall temperatures to increase slightly as a result of thermal gradients in the solid cylinder wall materials. We anticipate that this effect is negligible at the aluminium inner cylinder wall, but may be significant at the glass outer cylinder wall due to the much lower thermal conductivity of this material ($k_{glass} \sim 1.4\,\mathrm{W\,m^{-1}\,K^{-1}}$, $k_{aluminium} \sim 237\,\mathrm{W\,m^{-1}\,K^{-1}}$). Unfortunately the nature of the apparatus (i.e. rotating inner and outer cylinders, and the necessity of an optically transparent outer cylinder) makes it difficult to monitor and control the wall temperatures. Thus the reported temperatures are those

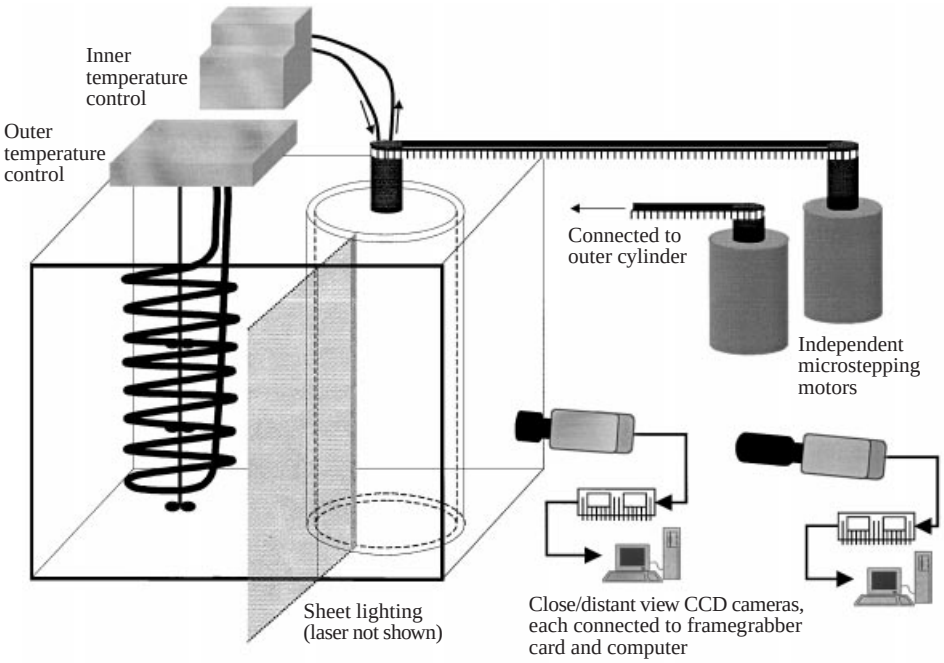

FIGURE 2. Schematic diagram of experimental apparatus.

of the thermostatting fluid and not necessarily the wall. We anticipate the temperature difference between the outer and inner cylinders to be small, always $< 2.5\,\mathrm{K}$, which is the temperature difference calculated when taking into account finite heat conduction within the outer cylinder at the maximum Na at which experiments were performed. In this calculation we have assumed rapid heat transfer from the exterior of the outer cylinder, i.e. that the Biot number $\gg 1$, which allows us to consider the exterior wall of the outer cylinder to be at the same temperature as the bath. In most experiments, the temperature difference between the outer and inner cylinders will be much smaller than 2.5 K. However, the results of Al-Mubaiyedh *et al.* (2002) suggest that even small temperature differences such as these may affect the symmetry of the disturbance flow.

2.2. *Illumination and imaging*

The fluid is seeded with a small amount (2×10^{-5} volume fraction) of mica flakes having major axes between 5 and 35 μm and thickness approximately 0.3 μm. This level of seeding resulted in no measurable changes in the fluid properties. Deviations of the fluid motion from purely azimuthal shearing motion, i.e. motion of the fluid in the (r, z)-plane, can be observed by differences in the intensity of light reflected from the anisotropic seeding particles. A beam of light from an argon ion laser is focused into a uniform sheet of light using a Powell lens; the sheet is co-planar with the z-axis of the cylinder, illuminating the entire gap. Two CCD cameras, placed orthogonal to the light sheet, capture images of light reflected from the moving seeding particles. One camera is used to provide a close-up view while the other is placed farther away to allow visualization of the entire gap. The images are stored in digital format on a computer and processed using *NIH Image* public domain software (Rasband 1994) to enhance the visibility of the often weak secondary flow structures. It is often convenient to represent an experiment with a single image. This can be done by

constructing a space–time plot, which is formed by extracting a central line of pixels from sequential digital images of the gap between the cylinders and stacking them vertically. These space–time plots or time sequences can be used to present concisely the bulk of the information available from the experiment. The time sequences are plotted with short times at the top and long times at the bottom, with the axial position increasing from left to right. Stationary structures appear as vertical streaks in the time sequence, while moving structures appear as slanted lines. For every experiment we generate both space–time plots and two-dimensional movies of the close-up and distant views in the (r, z)-plane. The movie images may be used to calculate information such as critical conditions, the time to onset of instability, and the axial wavenumber and frequency of the disturbance flow. Further details of both the apparatus and the image processing have been published in Baumert & Muller (1995).

2.3. *Time scales and determination of the critical conditions*

There are three important time scales involved in the non-isothermal Taylor–Couette flow of Newtonian fluids. The first is the time scale for diffusion of momentum across the gap between the cylinders, given by $\lambda_{viscous} = (R_2 - R_1)^2/\nu$. The Reynolds number may be thought of as the product of this time scale and shear rate, $Re = (\lambda_{viscous})(\dot{\gamma})$, where the shear rate is defined as $\dot{\gamma} = |\Omega_2 - \Omega_1|R_1/(R_2 - R_1)$. The second time scale is that for diffusion of vorticity from the ends of the cylinder to the centre, given by $\lambda_{end\ effect} = (L/2)^2/\nu$, where L is the axial length of the TC cell. This time scale is important for determination of how the end effects disturb the flow. Experimental TC apparatus typically has a very large aspect ratio and thus $\lambda_{end\ effect}$ is usually much larger than $\lambda_{viscous}$. The third time scale is a viscous heating time scale, given by $\lambda_{thermal} = (R_2 - R_1)^2/\alpha$, where α is the thermal diffusivity. This time scale, representing the time for Taylor–Couette flow to attain a steady temperature profile under the action of viscous heating, is typically quite large in comparison with the viscous time scale. The thermal time scale appears in the dimensionless Péclet number, $Pe = (\lambda_{thermal})(\dot{\gamma})$, which is also equal to the product of Re and Pr. For fluids with $Pr \gg 1$ flowing in high-aspect-ratio TC geometries, $\lambda_{viscous} < \lambda_{end\ effect} < \lambda_{thermal}$. Thus, we anticipate flow structures caused by inertia alone to respond at the most rapid time scale, flows caused by end effects to respond more slowly, and thermally influenced flows to respond slowest of all. In addition, secondary flows due to end effects will gradually propagate into the gap from the ends of the cylinders over the end-effect time scale, whereas secondary flows caused by either the inertial or thermal instabilities will be manifested in the appropriate time scale simultaneously throughout the gap.

Two types of Taylor–Couette experiments were performed to study the instability and determine the critical conditions. In step tests, one of the cylinders was accelerated from rest to its final angular velocity over the course of a few seconds and the evolution of the disturbance flow at constant velocity (and Re) was then monitored. These experiments provide information about the time scales present in the system, allow rough estimates of the stability boundaries, and are a convenient means for observing the temporal dynamics of the flow at fixed Reynolds number.

Once the appropriate time scales for the flow were confirmed through step tests, ramp tests were performed to determine the critical conditions. In ramp tests, the evolution of the disturbance flow was monitored as the angular velocity of one of the cylinders was increased at a slow, constant rate. Determination of the appropriate ramp rates is discussed in detail in § 3.4.

	a		Reference value		
	Glycerin	Solution	Glycerin	Solution	Correlation
η (Pa s)	7.42×10^3	6.43×10^3	0.952	0.270	$\eta = \eta_0 \exp[a(1/T - 1/T_{ref})]$
ρ (kg m^{-3})	−0.696	−0.458	1261	1241	$\rho = \rho_0 + a(T - T_{ref})$
C_p (J kg^{-1} K^{-1})	6.43	5.95	2417	2536	$C_p = C_{p0} + a(T - T_{ref})$
k (W m^{-1} K^{-1})	9.0×10^{-5}	0	0.285	0.295	$k = k_0 + a(T - T_{ref})$

TABLE 1. Parameters used to fit the temperature dependence of viscosity, density, heat capacity and thermal conductivity for pure glycerin and the 93.3% glycerin–6.7% water solution. T is expressed in Kelvin, $T_{ref} = 298$ K.

Fluid	ν (m^2 s^{-1})	η (Pa s)	ρ (kg m^{-3})	C_p (J kg^{-1} K^{-1})	k (W m^{-1} K^{-1})	Pr
83% glycerin–17% water	5.72×10^{-5}	0.0689	1204	2670	0.222	829
78% glycerin–22% water	2.79×10^{-5}	0.0335	1198	2815	0.330	286
Butene oligomer	1.59×10^{-3}	1.47	925.2	1909	0.145	19 350

TABLE 2. Properties of fluids studied at a single temperature.

2.4. *Test fluids*

In order to cover a broad range of *Re* and *Na*, several Newtonian fluids were studied in this work. Three fluids were studied at a single temperature of 300 K: two low-viscosity glycerin–water solutions (83% glycerin–17% water and 78% glycerin–22% water) and a highly viscous polybutene oligomer (40% Exxon Parapol 450, 60% Exxon Parapol 700). While changing the test fluid in the Taylor–Couette cell allows different parameter ranges to be accessed, it is laborious and time-consuming. For this reason, two other fluids, whose properties could be varied systematically and accurately by changing the temperature of the apparatus, were also studied. These two fluids were pure glycerin and a slightly less-viscous glycerin–water solution (93.3% glycerin–6.7% water).

The kinematic viscosity (ν) of the fluids was determined by capillary viscometry as a function of temperature for the temperature range accessible in the Taylor–Couette cell: 286–317 K. The density (ρ) as a function of temperature was also determined experimentally. The experimental values of kinematic viscosity and density were used to calculate the shear viscosity (η) at each temperature for the fluids. The heat capacity (C_p), and thermal conductivity (k) of the fluids were estimated using literature values (Miner & Dalton 1953; Incropera & De Witt 1990). The fluid properties were fit to linear functions of temperature for the density, heat capacity and thermal conductivity, and an exponential Arrhenius-type function for the viscosity. These functions can be used along with the experimental rotation speed and geometrical parameters to calculate the dimensionless parameters describing the flow in the Taylor–Couette apparatus. Table 1 reports the correlations used to fit the fluid property–temperature relationships for the pure glycerin and the 93.3% glycerin–6.7% water solution. Table 2 reports the properties of the glycerin–water solutions and polybutene oligomer, determined as above but at the single temperature at which those fluids were studied in the Taylor–Couette cell. The values of Γ, the thermal sensitivity of the viscosity, and β, the volumetric thermal expansion coefficient, are

Fluid	Γ	$\Gamma/T\,(\mathrm{K}^{-1})$	$\beta\,(\mathrm{K}^{-1})$
Glycerin, $T = 289\,\mathrm{K}$	25.7	8.91×10^{-2}	5.50×10^{-4}
Glycerin, $T = 300\,\mathrm{K}$	24.8	8.26×10^{-2}	5.53×10^{-4}
Glycerin, $T = 311\,\mathrm{K}$	23.9	7.68×10^{-2}	5.57×10^{-4}
93.3% glycerin–6.7% water, $T = 289\,\mathrm{K}$	22.3	7.72×10^{-2}	3.68×10^{-4}
93.3% glycerin–6.7% water, $T = 300\,\mathrm{K}$	21.5	7.16×10^{-2}	3.69×10^{-4}
93.3% glycerin–6.7% water, $T = 311\,\mathrm{K}$	20.7	6.66×10^{-2}	3.71×10^{-4}
Butene oligomer, $T = 300\,\mathrm{K}$	24.1	7.99×10^{-2}	6.59×10^{-4}

TABLE 3. Thermal sensitivity of viscosity and density for pure glycerin, the 93.3% glycerin–6.7% water solution, and the butene oligomer.

Fluid	$\lambda_{viscous}$ (s)	$\lambda_{end\ effect}$ (s)	$\lambda_{thermal}$ (s)
Glycerin, $T = 289\,\mathrm{K}$	0.0267	24.6	470
Glycerin, $T = 300\,\mathrm{K}$	0.0689	63.4	480
Glycerin, $T = 311\,\mathrm{K}$	0.166	153	489
93.3% glycerin–6.7% water, $T = 289\,\mathrm{K}$	0.103	94.8	468
93.3% glycerin–6.7% water, $T = 300\,\mathrm{K}$	0.234	216	479
93.3% glycerin–6.7% water, $T = 311\,\mathrm{K}$	0.502	462	489
Butene oligomer, $T = 300\,\mathrm{K}$	0.109	25.9	2109

TABLE 4. Viscous, end-effect, and thermal time scales for pure glycerin, the 93.3% glycerin–6.7% water solution, and the butene oligomer.

reported in table 3 for pure glycerin, the 93.3% glycerin–6.7% water solution, and the butene oligomer. The values of β and Γ for the multi-temperature fluids are reported at three temperatures representing the lowest, middle, and highest used in the experiments. For the butene oligomer, β and Γ at the single temperature 300 K are reported based on measurements of ρ and η as a function of temperature near 300 K. Values of Γ/T, which are more directly comparable to values of β for the fluids, are also reported in table 3. It is important to note that the thermal sensitivity of the viscosity is two orders of magnitude larger than the thermal sensitivity of the density for all fluids.

This choice of fluids, studied over the temperature range 286–317 K, allows the viscosity to vary over the range 0.0333 to 2.12 Pa s. For the possible cylinder rotation speeds of our apparatus, this allows *Re* to vary from 0 to 164 and *Na* to vary from 0 to 2.01. For the fluids studied here, the three time scales for non-isothermal Taylor–Couette flow vary according to the general progression proposed in § 2.3, i.e. $\lambda_{viscous} < \lambda_{end\ effect} < \lambda_{thermal}$. The viscous time scale, $\lambda_{viscous} = (R_2 - R_1)^2/\nu$, is on the order of 0.1 s for all fluids. The end-effect time scale, $\lambda_{end\ effect} = (L/2)^2/\nu$, is a factor of 240 or 920 times larger than $\lambda_{viscous}$ for fluid flow in the wider or narrower geometries, respectively. The thermal viscous-heating time scale, $\lambda_{thermal} = (R_2 - R_1)^2/\alpha$, is on the order of 500 s for the fluids studied in the narrower geometry, and 2000 s in the wider geometry. A list of the time scales for pure glycerin, the 93.3% glycerin–6.7% water solution, and the butene oligomer is given in table 4. The time scales for the multi-temperature fluids are reported at three temperatures representing the lowest, middle, and highest used in the experiments.

For Taylor–Couette flow in the presence of viscous heating, the temperature will vary with radial position in the gap. This temperature stratification will result in gradients in thermally sensitive fluid properties. Throughout this paper, we report

flow parameters in terms of fluid properties evaluated at the controlled thermostatting bath temperature T_0.

2.5. *Experimental uncertainty*

As in any experimental study, there are uncertainties in both the estimation of physical properties of the test fluids and in the measurement of onset conditions from our image data. We have performed an error analysis and the error bars are included on the figures in which we present quantitative data. In this section, we discuss our primary sources of error. The control of the temperature of the outer and inner cylinders is the largest source of error in this study. Temperature is the key experimental variable because a small change in temperature will have a large effect on the fluid properties, primarily the viscosity. While the temperature of the fluids in the circulator reservoirs is controlled to within ± 0.1 K, at temperatures far from room temperature, heat transfer from connecting hoses and the non-submerged parts of the TC cell occurs. This results in larger errors in experiments performed at the temperature extremes. This uncertainty in temperature was measured in independent runs in which the circulating fluid temperature could be measured at several points in the apparatus. There is also a certain amount of subjectivity in determining onset times and critical conditions from image data. A generous allowance in the error analysis was made for this uncertainty. We have also included in our error analysis the uncertainties in the measurement or estimation of R_1, R_2, k, C_p, η, and ρ. The effects of these uncertainties are small in comparison with the other sources of error discussed. We anticipate that other factors, such as buoyancy and end effects, will have an influence on the stability characteristics of the flow. It is beyond the scope of our study to include these effects in our error analysis, however, because to fully account for them a full theoretical stability analysis must be undertaken.

3. Results and discussion

3.1. *General properties of the new instability*

Preliminary experiments in the narrower gap geometry with the lowest-viscosity glycerin–water mixture (78% glycerin) confirmed the rapid onset of stationary, axisymmetric vortices at a critical Reynolds number within 0.4% of the predictions of isothermal linear stability theory for the case of rotation of the inner cylinder with the outer cylinder held stationary. These tests, which were rapid ramps of a very low-viscosity solution, have a vanishingly small Nahme–Griffith number ($Na = 2.47 \times 10^{-3}$) and are thus assumed to represent the isothermal Taylor instability. The wider gap geometry was also tested with a low-viscosity glycerin–water mixture (83% glycerin) and the transition to Taylor vortices occurred within 2% of the predictions for isothermal linear theory. Here the Nahme–Griffith number is very low ($Na = 4.26 \times 10^{-3}$) and once again we assume this represents the isothermal Taylor instability in the wider geometry. We propose that the agreement is better in the narrower case than the wider due to a reduction of end effects. For this reason, the majority of our experiments were performed in the narrower geometry.

With fluids having a higher viscosity a transition to secondary flow is observed at Reynolds numbers well below the critical Reynolds number for the isothermal, inertial instability ($Re_{c,iso}$). These secondary flow structures are oscillatory axisymmetric vortices that develop only after a long period of shearing and are much weaker than the base flow. These features are in contrast to the well-characterized isothermal Taylor instability, where the disturbance flow develops on the very rapid viscous time

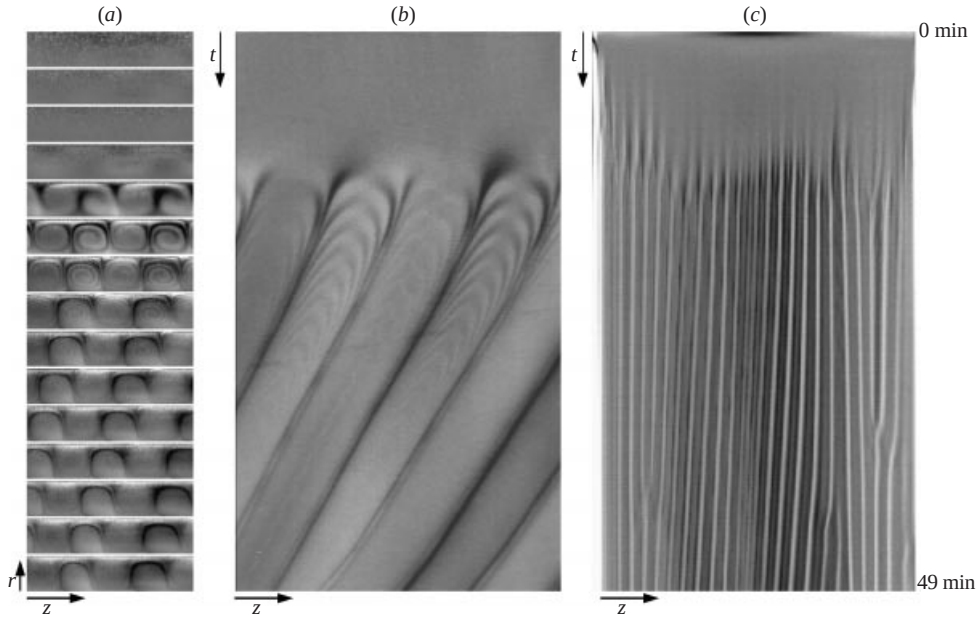

FIGURE 3. Images representing the (r, z)-plane of Taylor–Couette flow of glycerin at $\dot{\gamma} = 271\,\mathrm{s}^{-1}$, $Re = 12.0 = 0.086Re_{c,iso}$, $Na = 1.26$, $Pe = 129\,000$, in the narrower geometry ($R_1/R_2 = 0.912$) with the inner cylinder rotating. (a) Cross-sectional-view images: the inner cylinder is at the bottom and the outer cylinder at the top. (b) Close-up-view space–time plot. Extent of the z-axis is 4.71 gap widths. (c) Distant-view space–time plot. Extent of the z-axis is 57.8 gap widths. In these and all subsequent images, height (z-axis) increases to the right.

scale and the secondary flow is stationary and of comparable strength to the base flow.

While certain properties of this instability, such as onset times, temporal frequencies and vortex strengths, vary widely depending on the flow conditions, many features of this instability are universal. Example images of the onset of the disturbance flow in the (r, z)-plane and close-up and distant-view space–time plots of the 'typical' instability following a velocity step test in the narrower geometry are given in figure 3. Here, at $Re = 12.0 = 0.086Re_{c,iso}$, $Na = 1.26$, a secondary vortex flow forms approximately 10.6 min after the start of shearing. The vortices move downward in the gap at a frequency of $0.0081\,\mathrm{s}^{-1}$. This corresponds to a vortex propagation velocity of 0.0032 gap widths s^{-1}, a rate that is very slow compared with the rotation speed of the inner cylinder (4.151 revolutions s^{-1}). The distant-view time sequence shows that the instability starts fairly uniformly across the entire gap and further demonstrates that the vortex propagation velocity is very slow. The long time scale for the onset of instability is typical of all instabilities of this type, and is consistent with the long thermal time scale for this flow. The vortices travelling downward in the gap is also a typical feature of this instability. The time for onset of the instability decreases and the vortex propagation speed increases as the rotation speed is increased (and thus both Re and Na are increased). The disturbance flows appear axisymmetric in all experiments; in selected cases this has been confirmed by ambient time-sequence capture and subsequent FFT analysis. A detailed description of our tests for non-axisymmetry can be found in Baumert & Muller (1999).

To gain insight into the mechanism of the instability, we present experiments

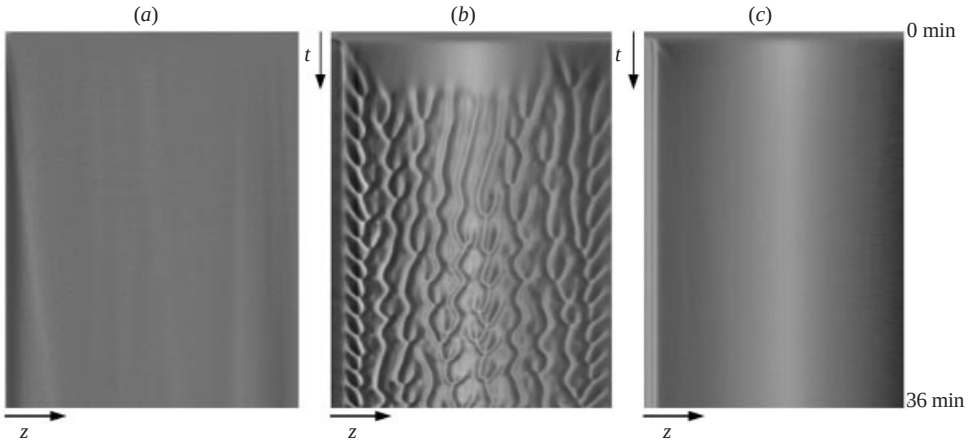

FIGURE 4. Space–time plots at $Re/Re_{c,iso} = 0.179$ in the wider geometry ($R_1/R_2 = 0.827$). (*a*) 83% glycerin–17% water, $\dot{\gamma} = 6.0\,\mathrm{s}^{-1}$, $Na = 1.42 \times 10^{-4}$, with inner cylinder rotating. (*b*) Glycerin, $\dot{\gamma} = 112.8\,\mathrm{s}^{-1}$, $Na = 0.914$, with inner cylinder rotating. (*c*) Glycerin, $\dot{\gamma} = 112.8\,\mathrm{s}^{-1}$, $Na = 0.914$, with outer cylinder rotating. The extent of the z-axis is 30 gap widths in each image.

with pure glycerin and with the 83% glycerin–17% water solution in the wider geometry. Experiments with the glycerin–water mixture, which has a much lower viscosity than pure glycerin, show that this low-Nahme–Griffith-number flow does not exhibit instability. With this fluid, at all $Re < Re_{c,iso}$, the flow remains purely azimuthal, as illustrated by the distant-view space–time plot shown in figure 4(*a*). Here, at $Re = 0.179Re_{c,iso}$, $Na = 1.42 \times 10^{-4}$, and $Pr \approx 830$, the featureless nature of the plot reveals the absence of any stationary or moving structures in the gap, consistent with direct examination of the images of the gap. A space–time plot of the same experiment as in figure 4(*a*) but for the more-viscous glycerin, for which $Na = 0.914$ and $Pr \approx 11\,000$, is shown in figure 4(*b*): the outer cylinder is held fixed and the inner cylinder is accelerated from rest to a value corresponding to $0.179Re_{c,iso}$ in a few seconds. A purely azimuthal base flow is initially established but is replaced after about 5.3 min by axisymmetric, axially travelling vortices. Here the vortices travel axially and merge with other vortices during the course of the experiment. A comparison of figures 4(*a*) and 4(*b*) indicates that the vortex flow is due to destabilization of the centrifugal instability by viscous heating effects. That this disturbance flow is not driven solely by buoyancy induced by viscous heating is demonstrated by figure 4(*c*); here we show an experiment at the same Re, Na, and Pr as figure 4(*b*), but with centrifugal destabilization absent since the flow is generated by rotation of only the outer cylinder.

The experiments pictured in figure 4 indicate that the new, oscillatory mode of instability in Newtonian TC flow at low Reynolds numbers occurs only above some critical Nahme–Griffith number, and only when centrifugal destabilization of the flow is present. Thus, the instability appears to be due to a coupling between viscous dissipation-induced temperature stratification and centrifugal destabilization (White & Muller 2000). The observed destabilization of Newtonian TC flow by viscous heating is consistent with the work of Al-Mubaiyedh *et al.* (1999, 2002). The change in the spatio-temporal character of the disturbance flow from stationary to oscillatory is consistent with their calculations in which the outer cylinder wall is assumed to be slightly hotter than the inner cylinder wall.

A distant-view time-sequence plot of a linear ramp in cylinder rotation rate in the wider geometry for the oligomeric butene fluid is shown in figure 5. This figure serves a dual purpose: it demonstrates that similar instabilities occur in fluids other than glycerin-based solutions, and also shows concisely the flow behaviour as the rotation speed is increased above the critical rotation speed. Here, increasing rotation speed increases all of the destabilizing parameters Re, Na, and Pe simultaneously; Re and Pe increase linearly with time, while Na increases quadratically with time. (We present experiments below where we change only Na and Pe while holding Re fixed.) At the beginning of this ramp, which starts at $Re = 1.31$, $Na = 2.03 \times 10^{-2}$, $Pe = 25\,400$, there is no secondary flow. At $Re = 8.94$, $Na = 0.942$, $Pe = 173\,000$, axisymmetric, oscillatory secondary flow structures appear. Again, this Reynolds number is well below $Re_{c,iso} = 101.56$, the critical Reynolds number for the isothermal Taylor instability in this geometry. The vortices move slowly downward and as the rotation rate of the inner cylinder is increased, the vortex propagation speed increases. Eventually the vortices display more chaotic behaviour as they oscillate axially and merge with one another. Although the flow varies in the axial direction, it remains axisymmetric. This progression of features is seen in all types of fluids studied as the destabilizing parameters are increased above the critical conditions in the wide gap apparatus. In the narrow gap geometry, the progression of structures is always from purely azimuthal flow to ordered, axisymmetric vortices that move steadily down the axis of the cylinders, as seen in figure 3. The disordered, merging vortices seen in figure 4(b) and at the bottom of figure 5 were not observed in the narrow geometry.

As the thermal properties (k, C_p) of this oligomeric butene fluid were not readily available and had to be estimated, we chose to perform a more comprehensive exploration of the properties of this instability with better-characterized glycerin-based fluids.

3.2. *Step tests: effects of co-rotation*

In an effort to elucidate the relevant time scales and stability boundaries for this instability, more systematic experiments were performed in the narrower geometry. The narrower geometry was chosen because it is less sensitive to end effects due to the larger aspect ratio. Also, since it is impossible to completely eliminate the effects of buoyancy from the experiments, we prefer the narrower gap to keep buoyancy effects to a minimum.

Here we describe tests performed to investigate the effects of co-rotation on this new, oscillatory instability. In the isothermal Taylor–Couette problem, the first instability to Taylor vortices is driven by centrifugal destabilization and so increasing the amount of co-rotation of the outer cylinder results in additional destabilization of the base flow. Regardless of the amount of co-rotation, the first transition is always to stationary, axisymmetric vortices. For the present radius ratio, as the co-rotation parameter $B = (\Omega_2 - \Omega_1)/\Omega_1$ is increased from -1 (corresponding to a stationary outer cylinder) towards -0.558 (the largest amount of co-rotation considered here), the critical Reynolds number $Re = |\Omega_2 - \Omega_1| R_1(R_2 - R_1)/\nu$ decreases monotonically by approximately 33% (cf. Chandrasekhar 1961). Since, as demonstrated in figure 4, centrifugal destabilization is also critical to this new viscous-heating-induced instability, we anticipate that co-rotation will enhance destabilization of this new mode.

To assess these effects, the outer/inner cylinder co-rotation was varied at a fixed shear rate. Because the shear rate is the same in each of the experiments, the Nahme–Griffith number and thus the temperature increase and subsequent change in fluid properties due to viscous heating will be the same. The Reynolds number as we define

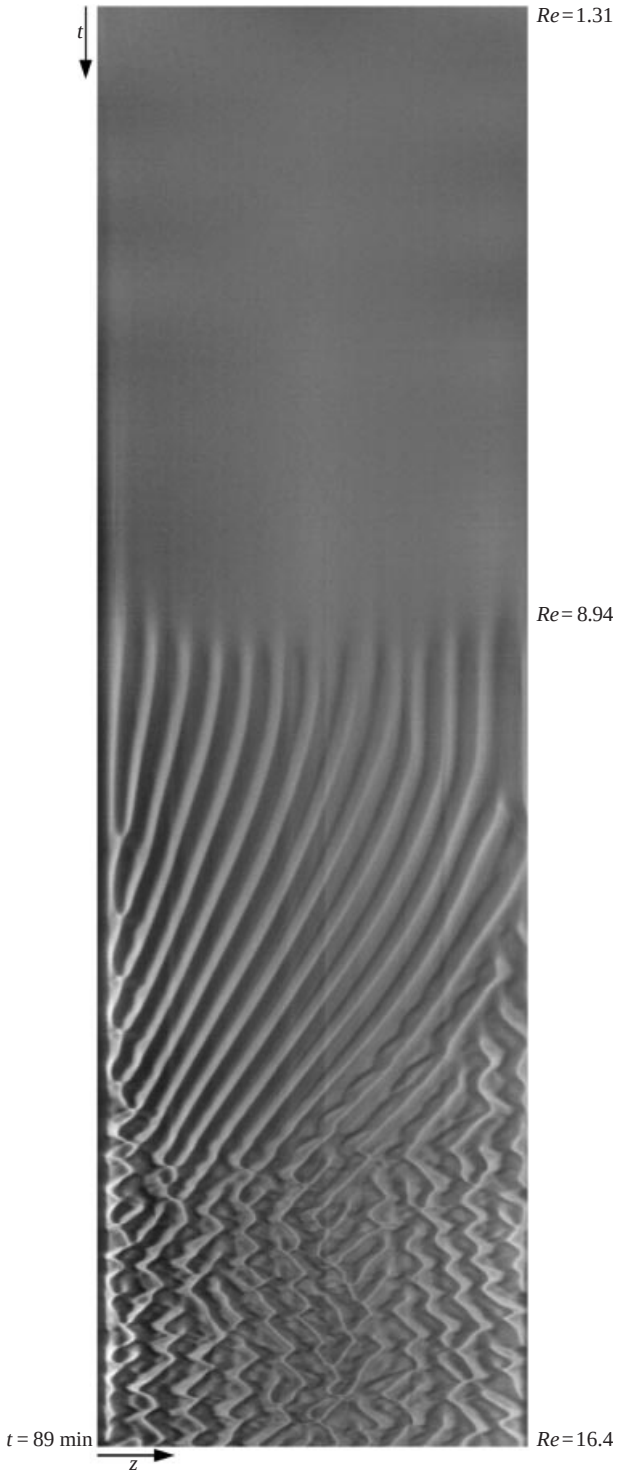

FIGURE 5. Space–time plot representing a velocity ramp of inner cylinder rotation rate with the butene oligomer in the wider geometry ($R_1/R_2 = 0.827$). The outer cylinder is stationary. The extent of the z-axis is 29.7 gap widths.

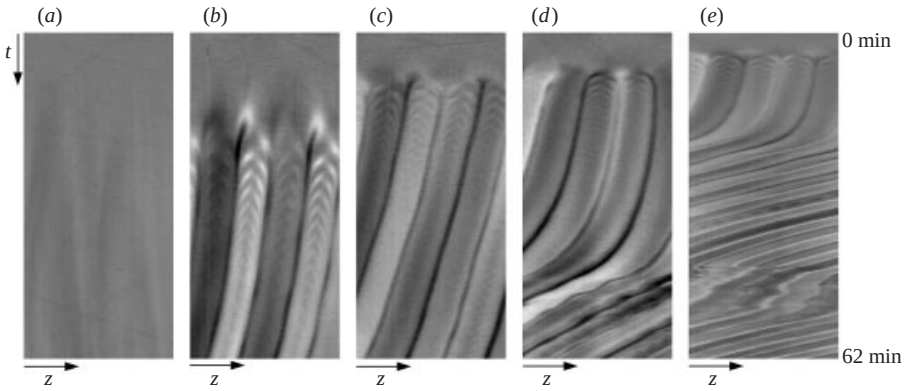

FIGURE 6. Space–time plots of glycerin, all at $Re = 19.1 = 0.136Re_{c,iso}$, $Na = 0.573$, $Pe = 119\,000$, with varying co-rotation of the outer cylinder. (*a*) $B = -1$, (*b*) $B = -0.883$, (*c*) $B = -0.809$, (*d*) $B = -0.680$, (*e*) $B = -0.558$. The extent of the z-axis is 4.8 gap widths in each image. In this and all subsequent figures the narrower geometry is used ($R_1/R_2 = 0.912$).

it is also constant throughout the experiments, but the centrifugal destabilization increases as B is increased from -1 towards -0.558. Using pure glycerin as the working fluid, both of the cylinders were accelerated from rest to their final velocity over the course of a few seconds at the start of the experiment and the evolution of the flow at constant Re was monitored.

Figure 6 shows close-up-view time sequences for a series of experiments at the same shear rate corresponding to $Re = 19.1 = 0.136Re_{c,iso}$, $Na = 0.573$, and $Pe = 119\,000$. The amount of centrifugal destabilization varies with increasing outer cylinder co-rotation, increasing from left (*a*) to right (*e*) in the figure. In figure 6(*a*), there is no outer cylinder co-rotation and no secondary flow is apparent in 90 min of shearing. As B is increased from -1 towards -0.558, instabilities occur and the onset times become progressively smaller as seen in figure 6(*b–e*). In addition, the axial propagation speed of the vortices increases as the outer cylinder co-rotation is increased. The onset times, scaled with the thermal time scale $\lambda_{thermal}$, are plotted versus the co-rotation parameter B in figure 7. These experiments show that the time-dependent nature of the instabilities depends on the amount of both viscous heating and centrifugal destabilization present in the experiment. We explore the role of the destabilizing effects of viscous heating and inertia on the time scale for onset of the instability in the next section.

3.3. *Step tests: probing the time scale for instability*

More accurate determination of the critical conditions for the instability requires gradual ramps in Reynolds number. However, in order to verify our estimates of various time scales (important in determining appropriate ramp rates) and to confirm the absence of other, longer time scales, step tests were first undertaken. As in § 3.2, one of the cylinders was accelerated from rest to its final velocity over the course of a few seconds at the start of the experiment and the evolution of the flow at constant Re was monitored. Throughout the remainder of this study, we restrict our attention to the case of a stationary outer cylinder, i.e. $B = -1$.

Several step tests at fixed Reynolds number and varying Nahme–Griffith number were performed. This was achieved by varying the experimental temperature (so that the viscosity would be changed) and adjusting the rotation rate such that the Re

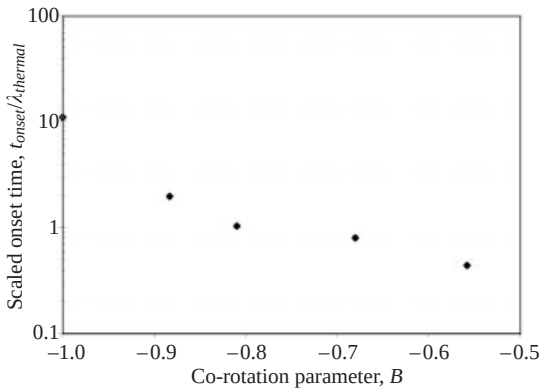

FIGURE 7. Onset time as a function of co-rotation parameter B for glycerin, all experiments at $Re = 19.1 = 0.136Re_{c,iso}$, $Na = 0.573$, $Pe = 119\,000$. Filled symbols exhibited a transition at the indicated time. The hollow symbol at $B = -1$ represents an experiment that ran for the indicated time and no discernable onset of secondary flow occurred. The error bars for these data are approximately the same size as the plotting symbols.

remained the same from one experiment to the next. Since Nahme–Griffith number depends differently on rotation rate than the Reynolds number, each experiment corresponds to flow at a different Nahme–Griffith number. The Péclet number ($Pe = Re\,Pr$) also varies due to the change in fluid properties with temperature. This process was repeated for several Reynolds numbers, using both the pure glycerin and the 93.3% glycerin–6.7% water solution.

The close-up-view time sequences from one set of these experiments are shown in figure 8, representing flows at $Re = 29.9 = 0.213Re_{c,iso}$. The first time sequence is devoid of any features and thus there is no transition to secondary flow in this experiment, which was run for 71 min. The next three experiments do show a transition to axisymmetric oscillatory vortices, and the time sequences in figure 8(b–d) show transitions at progressively smaller onset times as Na and Pe are increased. The vortex propagation velocity also increases substantially as Na increases at fixed Re. In step tests such as the ones shown in figure 8(b–d), an additional time after the onset of instability is required to attain the steady-state vortex propagation velocity. This is especially apparent in figure 8(d): although onset of instability occurs in 2 min, the slopes of the lines in this time sequence (and thus the axial propagation speed of the vortices) reach a steady value only after $\sim$ 8 min of shearing. The eventual attainment of a steady vortex propagation velocity after the onset of instability is typical of all step tests performed; the time to reach the steady value decreases as Nahme–Griffith number increases at fixed Re.

The results of all of the step tests are plotted as dimensionless onset time (onset time divided by $\lambda_{thermal}$) vs. Nahme–Griffith number in figure 9(a). This figure shows that at each Reynolds number the onset time decreases as Na increases, thus demonstrating that increasing the rate of viscous heating decreases the onset time for instability. The same rate of viscous heating (same Na) will result in a different onset time for flows with different amounts of centrifugal destabilization (different Re). However, if the data are plotted as dimensionless onset time vs. Péclet number as in figure 9(b), the curves at all of the Reynolds numbers investigated appear to collapse onto a single curve. This curve approaches a very high onset time as Pe is decreased to a value of approximately 120 000. Below this value of Pe, no instabilities were seen for

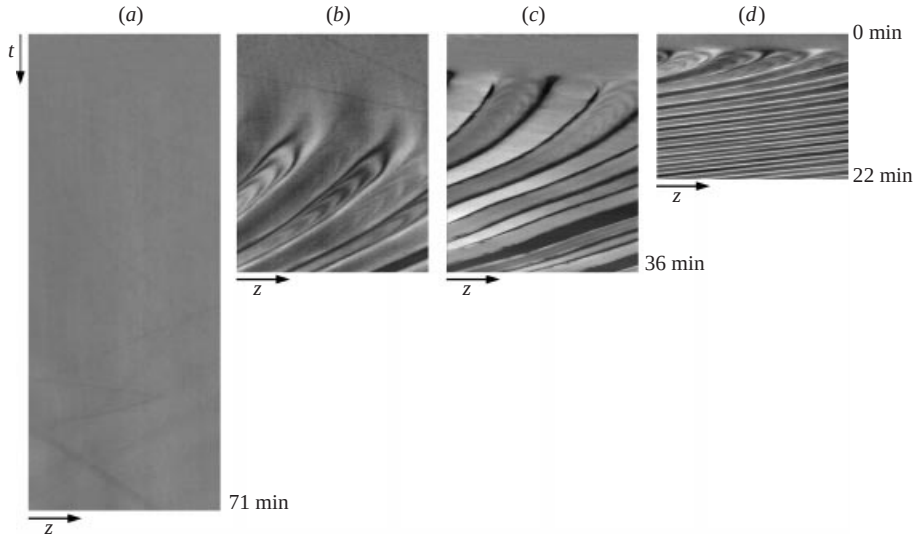

FIGURE 8. Space–time plots of glycerin at $Re = 29.9 = 0.213Re_{c,iso}$. (*a*) $Na = 0.436$, $Pe = 129\,000$. (*b*) $Na = 0.499$, $Pe = 134\,000$. (*c*) $Na = 0.703$, $Pe = 150\,000$. (*d*) $Na = 0.991$, $Pe = 167\,000$. The extent of the z-axis is 4.8 gap widths and the inner cylinder is rotating in each image.

all $Re < Re_{c,iso}$ for experiments running approximately 1 to 2 hours. We believe that there would be no transition to secondary flow even if these experiments had run for longer times.

Figures 9(*a*) and 9(*b*) show that for all of the step experiments, instabilities occur within a few multiples of $\lambda_{thermal}$. This supports the idea that the instability is caused by a coupling of viscous heating and centrifugal destabilization. The velocity profile will reach an approximately fully developed state on the order of a few seconds ($\sim \lambda_{viscous}$) after the onset of shearing and thus the centrifugal destabilization of the flow will be established quickly. However, all flows remain in the base state until some time on the order of $\lambda_{thermal}$, the time for the temperature profile to approach steady state under the action of viscous heating. If we decrease the amount of viscous heating at fixed *Re*, below some *Na* the fully developed (infinite time) temperature gradients will not be large enough to cause destabilization and thus we should see no secondary flows. This is consistent with the experimental data; we observe no secondary flows for a given *Re* even for very long experiments below a certain *Na*. If we increase the amount of viscous heating at fixed *Re*, the temperature gradients become large enough to cause destabilization even without the flow being fully developed thermally, which gives rise to the smaller onset times.

To preserve the clarity of figures 9(*a*) and 9(*b*), the error bars are shown for only one set of experiments, those at $Re = 29$. The experiments at this *Re* were performed far from room temperature and represent the worst case in terms of experimental uncertainty (cf. § 2.5). The experiments at $Re = 12$ have error bars of a similar size, but all other data have error bars of approximately the same size as the plotting symbols. While the uncertainties in the data in figure 9(*b*) are not large enough to consider the data to collapse to a single curve, our error analysis neglects factors such as buoyancy that undoubtedly have some influence on the onset times. For the purposes of the present study, then, we consider the curve shown in figure 9(*b*) to demonstrate the appropriate scaling of the onset time with flow variables. The sharp

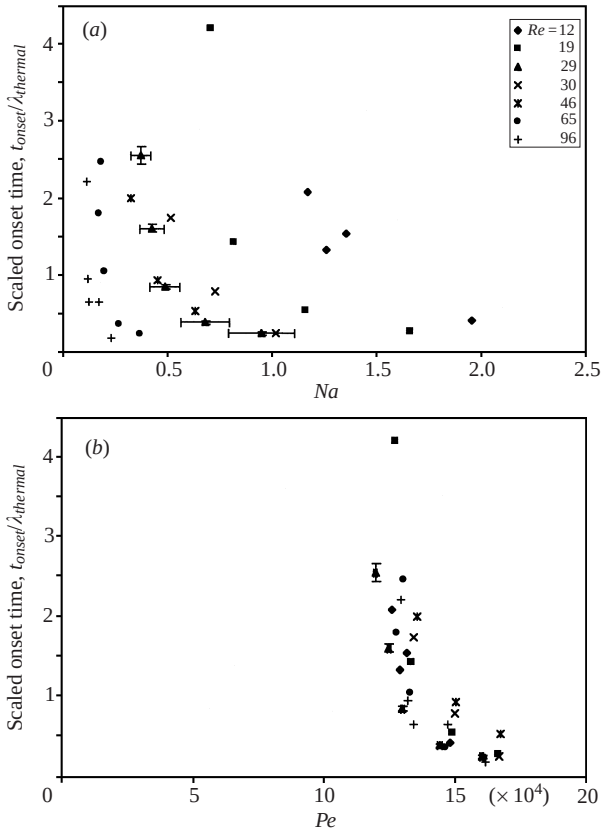

FIGURE 9. The onset time to instability for pure glycerin and 93.3% glycerin–6.7% water mixture, scaled by the thermal time scale: (*a*) vs. Nahme–Griffith number; (*b*) vs. Péclet number. All reported transitions are to axisymmetric oscillatory secondary flows that travel downward in the TC cell. Error bars for data at $Re = 12$ are comparable to those shown for $Re = 29$. For all other data sets, error bars are much smaller and approximately the same as the symbol size.

increase of onset time as Pe is decreased towards $Pe \approx 120\,000$ seen in figure 9(*b*) suggests that, at least over the range of parameters considered here, the instability happens at a critical Péclet number which is independent of Reynolds number. The curve in figure 9(*b*) provides a rationale for performing consistent ramp tests for different fluids (or temperatures). This is discussed more fully in the next section.

3.4. *Ramp tests*

While step tests are necessary to determine the time scales relevant to the instability, the critical conditions are best determined through slow ramp tests rather than through finite steps in rotation rate of the cylinders. Ramps in cylinder rotation rate allow one to achieve a large number of different flow states in the apparatus in a much shorter amount of time than step tests; however, careful attention must be given to the ramp rate when the flows are slowly developing. If, at a fixed rotation speed, the onset of instability takes several minutes, it is possible that the true critical condition may be reached and exceeded in a ramp before the instability is observed. This would cause over-estimation of the critical conditions. This can be avoided only by ramping at a rate that is slow compared to any time scale in the system, so that at each point in the ramp the flow and thermal fields are fully developed. Unfortunately,

the very long thermal time scales in this system made these 'pseudo-steady-state' ramps impractical.

Given the information from the step tests, however, we can adjust the ramp speed such that the time-dependent behaviour of the flow in each ramp is affected in the same way by the necessarily finite ramp speed. Figure 9(*b*) indicates that the instabilities at different Reynolds numbers have time scales that collapse, approximately, to the same curve of onset time vs. Péclet number. For this reason, the ramps were performed starting and ending at the same Pe while ramping in cylinder rotation rate such that the time rate of change of Péclet number, $\mathrm{d}(Pe)/\mathrm{d}t$, was the same for each ramp. With this procedure, the flow at each ramp speed will be given the same amount of relative time to reach instability. Thus the critical conditions obtained in such a manner will be comparable from ramp to ramp. While ramping at a finite rate may result in a slight over-prediction of the absolute critical conditions for the flow, it will allow us to make observations about how parameters such as Nahme–Griffith number, Reynolds number, and Péclet number interact to change the apparent critical conditions for finite ramp speed. These results can also be compared with theoretical predictions to see if the apparent critical conditions show the same dependence on flow parameters as the predicted critical conditions.

The ramp tests were performed by ramping the cylinders from $Pe = 100\,000$ to 160 000 at a rate $\mathrm{d}(Pe)/\mathrm{d}t = 16.0\,\mathrm{s}^{-1}$, using both the pure glycerin and the 93.3% glycerin–6.7% water solution. As in the step tests, we changed the properties of the fluid from ramp to ramp by adjusting the experimental temperature. A time sequence of the flow for each ramp was generated using the central 7.5% of the pixels in the movie images. Example space–time plots for three of the ramp experiments are shown in figure 10. The critical rotation speeds were determined from the time sequences, and these rotation speeds were used along with the fluid property data to calculate the critical values of Re, Na, and Pe. Note that as we continue the ramp above the critical conditions, the axial propagation velocity of the vortices increases with increasing Re and Na. This is especially obvious at the bottom of figure 10(*c*); as the ramp continues above Re_c the slope of the lines in the time sequence decreases until the lines are almost flat, which corresponds to the vortices moving very large axial distances in short times (i.e. a very high speed).

In three experiments at extremely low Na, the procedure above was modified slightly. For experiments with the 93.3% glycerin–6.7 % water solution at 313.7, 315.1 and 316.5 K, the critical condition for onset of instability lies near or below $Pe = 100\,000$. The ramps in this case were conducted from $Pe = 63\,000$ to 126 000 at 313.7 K, from $Pe = 58\,000$ to 121 000 at 315.1 K, and from $Pe = 53\,000$ to 116 000 at 316.5 K. All ramps are performed at the same ramp speed as used above, so that $\mathrm{d}(Pe)/\mathrm{d}t = 16.0\,\mathrm{s}^{-1}$.

The values of Re_c vs. critical Na are plotted in figure 11(*a*). As mentioned previously, a rapid ramp with a less viscous fluid (essentially isothermal flow) produced a secondary flow within 0.4% of the isothermal value for a Newtonian fluid. This would correspond to a point $Re_c = 140.2$, $Na \approx 0$. We do not include this point in figure 11(*a*), however, since this ramp was performed at a different ramp rate ($\mathrm{d}(Pe)/\mathrm{d}t = 27.6\,\mathrm{s}^{-1}$) than the rest of the data. Figure 11(*a*) shows that increasing Nahme–Griffith number (i.e. increasing viscous heating) dramatically destabilizes Newtonian Taylor–Couette flow. At $Na \approx 2$, the critical Reynolds number has dropped to less than 5% of the isothermal value. This is a striking result considering that there is no externally imposed temperature gradient. This is a much larger effect than was seen in the experimental studies of Sorour & Coney, where externally

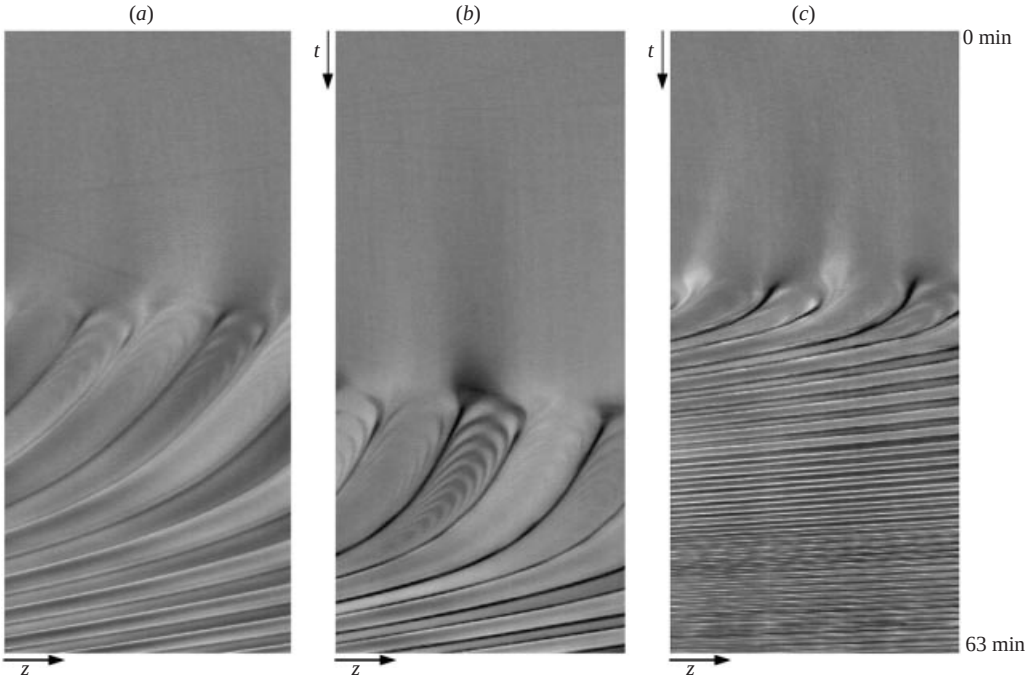

FIGURE 10. Space–time plots of selected ramp experiments used to determine apparent critical conditions in the narrower geometry. Ramps were conducted from $Pe = 100\,000$ to $160\,000$ at a rate $\mathrm{d}(Pe)/\mathrm{d}t = 16.0\,\mathrm{s}^{-1}$. (*a*) Glycerin, 291.5 K, $Re = 7.2$ to 11.6. Transition occurs at $Re = 9.1$, $Na = 1.64$, $Pe = 127\,000$. (*b*) Glycerin, 305.4 K, $Re = 22.2$ to 35.6. Transition occurs at $Re = 30.0$, $Na = 0.504$, $Pe = 135\,000$. (*c*) 93.3% glycerin–6.7% water, 305.4 K, $Re = 74.8$ to 119.6. Transition occurs at $Re = 92.4$, $Na = 0.120$, $Pe = 129\,000$. The span of the z-axis is 4.8 gap widths and the inner cylinder is rotating in each image.

imposed temperature differences of up to 16 K cause the critical Reynolds number to decrease only to 84% of the isothermal value.

Over the range of Na for which results for both fluids may be obtained, the curves are close to overlapping but the discrepancy exceeds slightly the experimental uncertainty. The pure glycerin displays critical Reynolds numbers consistently above those for the glycerin–water solution. Since the thermal expansion coefficient for glycerin is approximately 150% that of the glycerin–water solution, we speculate that the small discrepancy may be due to buoyancy. That is, for the glycerin, the same Nahme–Griffith number (and hence the same temperature difference across the gap) results in a higher Gr than for the glycerin–water solution, and these slight differences in buoyancy may give rise to the slight changes in the critical conditions reported.

The Péclet number at onset of instability is plotted versus Nahme–Griffith number in figure 11(*b*). This plot confirms the trend observed with the step tests: the instability appears to occur at a relatively constant value of Péclet number. (As in figure 11(*a*), the curves for the two different fluids do not collapse to the same curve, even when considering experimental uncertainty. Again, other influences such as buoyancy may affect the flow and result in these differences.) As Na approaches zero, however, a region where the critical Pe drops off precipitously is seen. This is the region where the isothermal critical condition is approached, and our strategy for performing ramp tests may not provide the same, consistent degree of over-prediction of the critical conditions at these very low Nahme–Griffith numbers as it does at higher Na. In

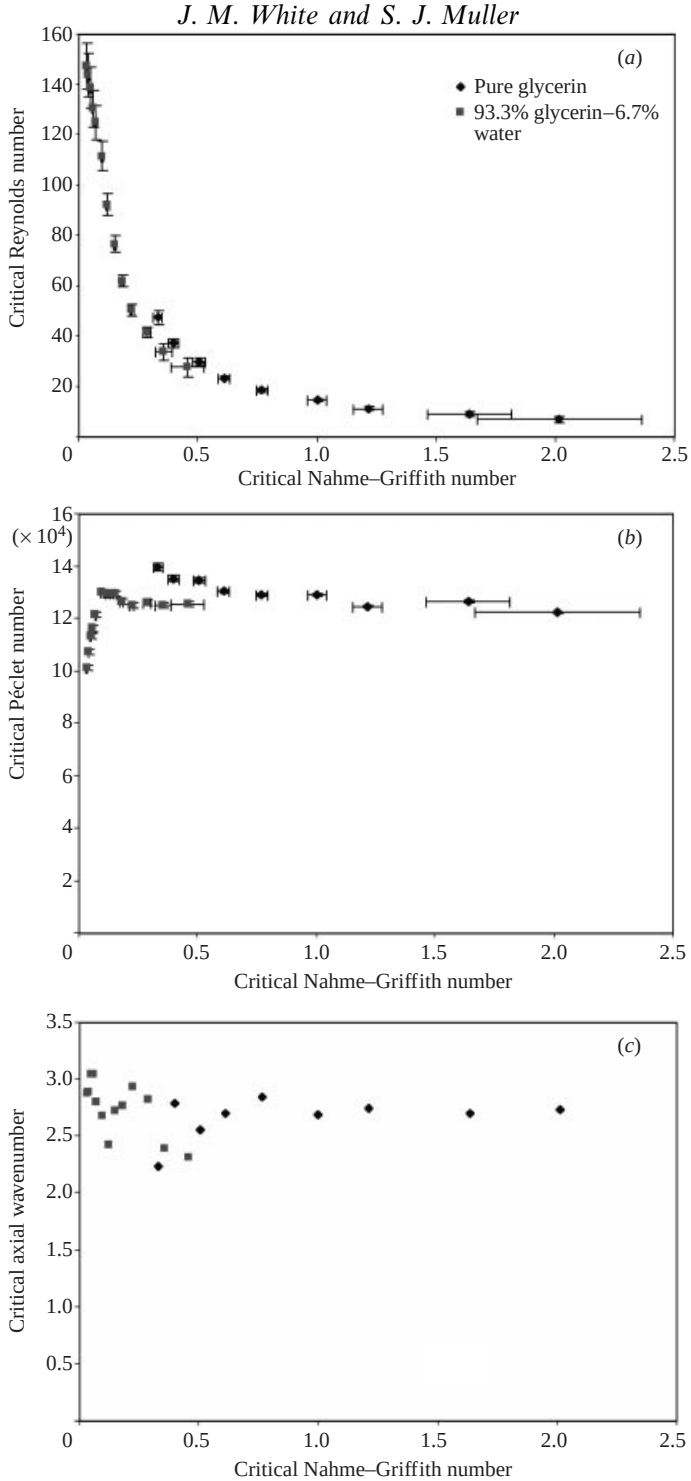

FIGURE 11. The apparent critical conditions for pure glycerin and 93.3% glycerin–6.7% water mixture, when the inner cylinder is ramped from $Pe = 100\,000$ to $160\,000$ at a rate $\mathrm{d}(Pe)/\mathrm{d}t = 16.0\,\mathrm{s}^{-1}$. (*a*) Critical Reynolds number vs. critical Nahme–Griffith number. (*b*) Critical Péclet number vs. critical Nahme–Griffith number. (*c*) Critical axial wavenumber vs. critical Nahme–Griffith number. All reported transitions are to axisymmetric oscillatory secondary flows that travel downward in the TC cell.

addition, as mentioned above, buoyancy effects become more important at these low *Na*; Grashof numbers based on both gravitational and centrifugal potentials are largest at $Na \sim 0.1$.

The critical axial wavenumber is plotted versus Nahme–Griffith number in figure 11(*c*). Here the axial wavenumber is defined as $2\pi(R_2 - R_1)/(\text{length of a vortex pair})$. These data were determined from the ramp images immediately after the onset of secondary flow. The critical axial wavenumber is relatively constant at ~ 2.7, with the wavenumbers at lower *Na* showing more scatter.

The first transition seen in the ramp experiments is always from the purely azimuthal base state to an axisymmetric vortex structure in which the vortices move slowly down the *z*-axis of the TC cell. The vortex propagation velocity (or frequency) at the critical condition can be determined from image data immediately after the onset of secondary flow. This frequency is approximately constant at $\sim 0.001\,\text{s}^{-1}$ for all experiments in which $Re_c < 105$. For experiments in which $Re_c > 105$, the frequency increases dramatically to $\sim 0.1\,\text{s}^{-1}$. The vortex propagation velocities show a lot of scatter, particularly at the lower Reynolds number flows. We believe the scatter is due to the difficulty in unambiguously determining the critical vortex propagation speed from ramp tests. As mentioned in the discussion of figure 8, for step tests in cylinder velocity a finite time is required after the initial onset of instability for the oscillatory vortices to reach a steady propagation speed. In a ramp test, the vortices also take time to reach their steady propagation speed. During this time, however, the rotation speed of the cylinders will be increasing due to the ramp, causing an increase in vortex propagation speed as seen at the bottom of figure 10(*c*). We report the values as near to the critical condition as possible, but the extent to which the ramp affects these measurements is unclear.

Experimental ramps at very low *Na*, achievable with the 93.3% glycerin–6.7% water solution at high temperatures ($T_0 > 308\,\text{K}$), can be performed at Reynolds numbers that approach and then exceed the isothermal critical condition, $Re_{c,iso}$, for the transition to Taylor vortex flow. In these experiments, the first transition is to the viscous-heating-induced oscillatory vortex flow. A second transition is then observed to Taylor vortex flow near $Re_{c,iso}$. Close-up-view time-sequence plots of such experiments at three different temperatures are shown in figure 12. In the ramp from $Re = 90.0$ to 144.0 at $T_0 = 308.15\,\text{K}$ shown in figure 12(*a*), there is a transition to oscillatory vortices at $Re = 111.5$. An abrupt transition to stationary Taylor vortices occurs at $Re = 131.2$. ($Re_{c,iso} = 140.2$ for this narrow gap apparatus; all *Re* reported here are based on fluid properties evaluated at the thermostatting bath temperature T_0.) These vortices are stationary but do move slightly as they settle into position. A transition to wavy Taylor vortices occurs at $Re = 143.0$. Since this is a non-axisymmetric flow structure, the vortices appear smeared as seen at the bottom of figure 12(*a*). Figure 12(*b*) shows a ramp from $Re = 77.6$ to 155.1 at $T_0 = 313.7\,\text{K}$. In this case, the transition to oscillatory vortices occurs at $Re = 138.8$. A transition to stationary Taylor vortices occurs at $Re = 145.2$. The ramp ended before a transition to wavy Taylor vortex flow was observed. Figure 12(*c*) shows a ramp from $Re = 77.1$ to 169.6 at $T_0 = 316.5\,\text{K}$. The transition to oscillatory vortices occurs at $Re = 147.5$, a transition to stationary Taylor vortices occurs at $Re = 151.3$, and a transition to wavy Taylor vortices at $Re = 167.2$.

The images in figure 12 show quite clearly that the oscillatory thermally induced instability precedes the formation of Taylor vortices at these *Na*. As the viscosity and hence Nahme–Griffith number is decreased, the range of cylinder rotation speed over which the oscillatory vortices may be observed decreases. As *Na* approaches

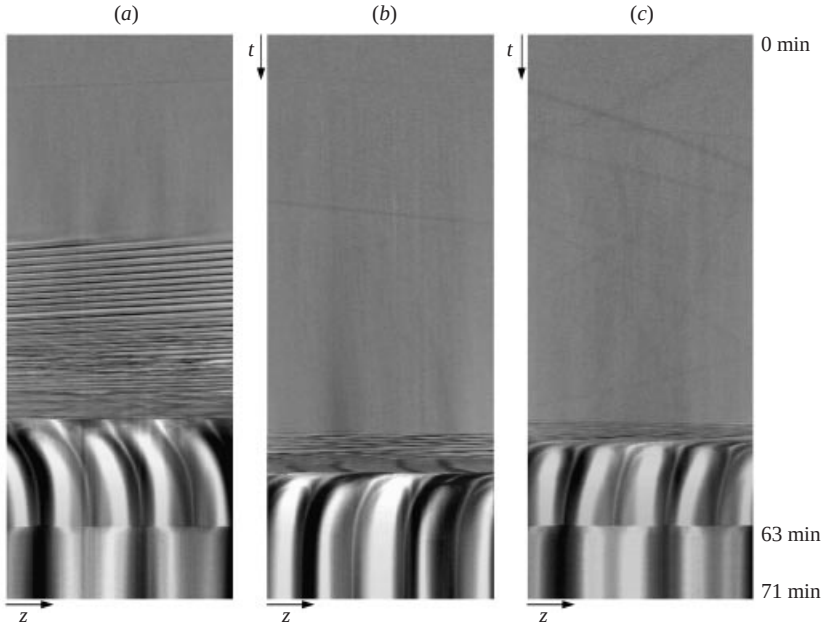

FIGURE 12. Space–time plots of ramp experiments of the 93.3% glycerin–6.7% water solution near the isothermal critical condition ($Re = 140.2$). The inner cylinder speed is ramped from 0 to the final value in 63 min, and the final rotation speed is held for an additional 8 min. (*a*) Ramp from $Re = 90.0$ to 144.0 at $T_0 = 308.15$ K. There is a transition to oscillatory vortices at $Re = 111.5$, $Na = 0.0973$. An abrupt transition to stationary Taylor vortices occurs at $Re = 131.2$. A higher transition to wavy Taylor vortices occurs at $Re = 143.0$. (*b*) Ramp from $Re = 77.6$ to 155.1 at $T_0 = 313.7$ K. The transition to oscillatory vortices occurs at $Re = 138.8$ and $Na = 0.0481$, and the transition to stationary Taylor vortices occurs at $Re = 145.2$. (*c*) Ramp from $Re = 77.1$ to 169.6 at $T_0 = 316.5$ K. The transition to oscillatory vortices occurs at $Re = 147.5$ and $Na = 0.0312$, a transition to stationary Taylor vortices occurs at $Re = 151.3$, and a transition to wavy Taylor vortices at $Re = 167.2$. The span of the z-axis is 4.8 gap widths and the inner cylinder is rotating in each image.

zero, the oscillatory transition will not occur and stationary Taylor vortex flow is the first observed transition, as in our preliminary experiments with the lowest-viscosity glycerin–water mixture. In this case, stationary Taylor vortices were observed at the predicted isothermal critical Re. It is not clear, however, whether stationary Taylor vortices are indeed the first transition at this small Na, or if there is a very narrow regime where oscillatory vortices occur, but the regime is so narrow it escapes detection.

In an effort to elucidate the nonlinear stability behaviour of this new mode, experiments were performed in which the inner cylinder speed was ramped through the critical condition from below (a ramp up) and from above (a ramp down). On the ramp up, Re_c is found as described above. The ramp down typically started at a Reynolds number 130% of Re_c. These experiments were performed with the 93.3% glycerin–6.7% water solution for several temperatures. In each case the critical Re determined from the ramp down is slightly less than Re_c determined from a ramp up. However, the differences between the two values of Re_c are small and within the uncertainty of the experiment. Thus, more precise experiments are necessary to determine whether the bifurcation is supercritical or weakly subcritical.

Preliminary comparisons of the linear stability theory of Al-Mubaiyedh *et al.* (2002)

with these experiments show good agreement. While these authors perform their linear stability analysis on glycerin with flow in a wider geometry ($R_1/R_2 = 0.827$) than the ramp experiments presented here ($R_1/R_2 = 0.912$), we can use these predictions for an initial, rough comparison. The magnitude of destabilization is in near-quantitative agreement with the ramp experiments shown in figure 11. At a Nahme–Griffith number of 2, both the experiments and predictions show $Re_c/Re_{c,iso} \approx 0.05$. The critical axial wavenumber is also comparable with the theoretical predictions. However, the linear theory predicts an axisymmetric stationary mode if the inner and outer wall temperatures are the same, while experimentally we observe axisymmetric oscillatory modes of instability. An oscillatory mode is predicted by Al-Mubaiyedh *et al*., however, if the imposed thermal boundary condition at the outer cylinder is 1.0 K hotter than the inner cylinder. This boundary condition may not be unrealistic since the outer cylinder of the apparatus is made of a low-thermal-conductivity glass. This outer wall may reach slightly higher temperatures than the aluminium inner wall when heat is generated in the fluid under the action of viscous dissipation. Predictions with this modification exhibit the observed temporal symmetry and the magnitude of destabilization is in semi-quantitative agreement with our experiments over the entire range of experimental data. In reality, we expect that any difference in wall temperatures will depend on the amount of heat generated and will thus vary with *Na* rather than remaining constant at 1.0 K. In addition, Al-Mubaiyedh *et al.* predict that under certain thermal boundary conditions, the bifurcation is subcritical. While our preliminary experiments to determine the nonlinear stability behaviour of the flow were inconclusive, a subcritical bifurcation would result in measured values of Re_c below those predicted by linear stability theory. We expect that with the proper choice of temperature difference between the outer and inner walls, or by imposing an appropriate outer-wall heat-flux boundary condition, and taking into account subcritical bifurcations, predictions for the narrow geometry will yield quantitative agreement with our experiments.

4. Conclusions

Here we have reported a new instability in the TC flow of Newtonian fluids that is caused by a coupling of viscous heating and centrifugal destabilization. The disturbance flow consists of axisymmetric toroidal vortices that are oscillatory and travel slowly down the vertical axis of the TC cell. This secondary flow is several orders of magnitude weaker than the base flow. Both the vortex propagation speed and the secondary flow strength increase substantially as the isothermal critical condition is approached (cf. figure 12). We attribute the lack of previous reports on this instability to the long time scales before the onset of secondary flow, to the high *Na* (i.e. very high viscosity) required to observe the instability, and to the weakness of the secondary flow. In addition, the window of conditions under which the oscillatory instability can be observed before the onset of Taylor vortex flow narrows considerably with decreasing *Na*; this may also have contributed to the lack of previous observation of this instability.

Step tests in cylinder velocity at fixed *Re* and *Na* but varying co-rotation parameter *B* demonstrate that increasing centrifugal force leads to increased destabilization of the flow. Step tests in cylinder velocity at fixed *Re* with varying *Na* indicate that the time for onset of instability is dependent on the Péclet number. The critical Péclet number at which the onset time diverges was found to be approximately 120 000. The onset times observed are consistent with the thermal time scale, i.e. the time for a

fluid under shear to attain a steady temperature profile under the influence of viscous heating.

Ramp tests in cylinder velocity confirm that the instability occurs at a nearly constant Péclet number of $\sim 120\,000$ if $Na > 0.1$ (i.e. if we are far enough away from the isothermal critical conditions). When the critical Reynolds number is plotted versus Nahme–Griffith number, the ramp tests reveal the large extent of destabilization as *Na* is increased. The magnitude of this destabilization is in agreement with the linear stability calculations of Al-Mubaiyedh *et al.* (2002), and the proper spatial and temporal symmetry is predicted under the assumption that the outer cylinder is slightly hotter than the inner.

We observe a 95% reduction from the isothermal critical Reynolds number for flow with a Nahme–Griffith number equal to 2.0. This *Na* corresponds to a maximum increase in temperature of 4.3 K in the fluid. Previous studies (Sorour & Coney 1979; Snyder & Karlsson 1964) show that externally imposed (linear) radial temperature gradients that cause buoyancy-induced destabilization of TC flows result in much more modest effects. Experiments with the largest imposed temperature gradients, studied by Sorour & Coney, show that temperature differences of up to 16 K cause only a 16% reduction from the isothermal critical *Re* for much less viscous oils. It is thus extremely important to consider viscous heating in hydrodynamic stability calculations and experiments, because unlike externally imposed temperature gradients and other modifications to the flow field, viscous heating is a function of fluid properties only and cannot be easily controlled or eliminated.

Finally, viscous heating effects are likely to be very important in the processing of high-viscosity polymeric materials. The current work may have considerable implications regarding the stability of flows of polymeric liquids. While polymer processing flows are typically destabilized by elasticity rather than inertia, our experiments with Newtonian fluids illustrate important ideas that can also be applied to the viscoelastic problem, where long time scales arise both due to viscous heating and due to the relaxation time of the polymer molecules. We are currently undertaking a detailed study of the TC stability of dilute polymer solutions to elucidate the effects of viscous heating on the elastic instability.

This work was supported in part by the Director, Office of Energy Research, Office of Basic Energy Sciences, Materials Sciences Division of the US Department of Energy under Contract No. DE-AC03-76SF00098. We would also like to thank U. Al-Mubaiyedh, R. Sureshkumar, and B. Khomami from Washington University for useful discussions regarding their theoretical results.

REFERENCES

Ali, M. & Weidman, P. D. 1990 On the stability of circular Couette flow with radial heating. *J. Fluid Mech.* **220**, 53–84.

Al-Mubaiyedh, U. A., Sureshkumar, R. & Khomami, B. 1999 Influence of energetics on the stability of viscoelastic Taylor–Couette flow. *Phys. Fluids* **11**, 3217–3226.

Al-Mubaiyedh, U. A., Sureshkumar, R. & Khomami, B. 2002 The effect of viscous heating on the stability of Taylor–Couette flow. *J. Fluid Mech.* **462**, 111–132.

Andereck, C. D., Liu, S. S. & Swinney, H. L. 1986 Flow regimes in a circular Couette system with independently rotating cylinders. *J. Fluid Mech.* **164**, 155–183.

Baumert, B. M. & Muller, S. J. 1995 Flow visualization of the elastic Taylor–Couette instability. *Rheologica Acta* **34**, 147–159.

Baumert, B. M. & Muller, S. J. 1999 Axisymmetric and non-axisymmetric elastic and inertio-elastic instabilities in Taylor–Couette flow. *J. Non-Newtonian Fluid Mech.* **83**, 33–69.

Chandrasekhar, S. 1961 *Hydrodynamic and Hydromagnetic Stability*. Oxford University Press.

Chen, J.-C. & Kuo, J.-Y. 1990 The linear stability of steady circular Couette flow with a small radial temperature gradient. *Phys. Fluids* A **2**, 1585–1591.

De Roquefort, T. A. & Grillaud, G. 1978 Computation of Taylor vortex flow by a transient implicit method. *Comput. Fluids* **6**, 259–269.

Incropera, F. P. & De Witt, D. P. 1990 *Fundamentals of Heat and Mass Transfer*. John Wiley and Sons.

Joseph, D. D. 1965 Stability of frictionally heated flow. *Phys. Fluids* **8**, 2195–2200.

Kolyshkin, A. A. & Vaillancourt, R. 1993 On the stability of non-isothermal circular Couette flow. *Phys. Fluids* A **5**, 3136–3146.

Koschmieder, E. L. 1993 *Benard Cells and Taylor Vortices*. Cambridge University Press.

Miner, C. S. & Dalton, N. N. 1953 *Glycerol*. Reinhold Publishing Corporation.

Rasband, W. 1994 *NIH Image*. National Institutes of Health. (Program available through anonymous FTP to zippy.nimh.nih.gov.)

Snyder, H. A. & Karlsson, S. K. F. 1964 Experiments on the stability of Couette motion with a radial thermal gradient. *Phys. Fluids* **7**, 1696–1706.

Sorour, M. M. & Coney, J. E. R. 1979 The effect of temperature gradient on the stability of flow between vertical, concentric, rotating cylinders. *J. Mech. Engng Sci.* **21**, 403–409.

Sukanek, P. C., Goldstein, C. A. & Laurence, R. L. 1973 The stability of plane Couette flow with viscous heating. *J. Fluid Mech.* **57**, 651–670.

Tagg, R. 1994 The Couette–Taylor problem. *Nonlinear Sci. Today* **4**(3), 1–25.

White, J. M. & Muller, S. J. 2000 Viscous heating and the stability of Newtonian and viscoelastic Taylor–Couette flows. *Phys. Rev. Lett.* **84**, 5130–5133.